

## Handheld Skin Printer: *In-Situ* Formation of Planar Biomaterials and Tissues

Navid Hakimi<sup>1</sup>, Richard Cheng, Lian Leng, Mohammad Sotoudehfar, Phoenix Qing Ba, Nazihah Bakhtyar, Saeid Amini-Nik<sup>\*</sup>, Marc G. Jeschke<sup>\*</sup>, Axel Günther<sup>\*</sup>

### S1. Materials and Methods

#### *Physical Characterization of Deposited Skin Substitutes*

Physical characterization of the deposited sheets included macroscopic measurements of sheet thickness, contact angle, for architected sheets the evaluation of stripe and spot sizes, as well as the elastic modulus. The microstructure was characterized by scanning electron microscopy (SEM) for  $n \geq 3$  samples.

#### *Sheet Thickness*

Precursor solutions were mixed with 5% 0.2  $\mu\text{m}$  diameter fluorescent microparticles (FP-0245-2 or FP-0256-2, Spherotech). Sheets were deposited onto flat agarose-coated square petri dishes (120 mm  $\times$  120 mm). The sheets were then cut into smaller sections, transferred onto microscope cover slides and imaged using an inverted laser-scanning confocal microscope (model A1, Nikon) or a digital camera (model Retiga 2000R Fast 1394, Q Imaging). The images were analysed using the ImageJ software (NIH, <https://imagej.nih.gov/ij/>). Sheet thickness obtained at 5 randomly selected points along the length on each sheet were evaluated for each experimental condition. The sheet thickness was also determined using an optical profilometer (model Contour GT-K, Bruker). Sheets were sectioned while attached to the agarose substrate and transferred to the profilometer stage. The Vision64 software program was used to analyze and export the sheet thickness data. 3D profile data were then imported into MatLab. Reported thickness data corresponded to local averages over a 0.5 $\times$ 0.5 mm<sup>2</sup> region of interest for each of the 5 sample points. For each experimental condition,  $n=3$  sheets were measured. **Figure S1** shows the individual processing steps. The flow rates that are used in this research for obtaining various thicknesses are derived from **Figure S9**.

#### *Contact Angle*

Using the microfluidic cartridge, we deposited sheets of alginate-collagen, fibrin-collagen and fibrin on agarose that were 10mm long, 14mm wide and 250 $\mu\text{m}$  thick. For comparison, a similar volume of fibrin-HA bioink, 35  $\mu\text{L}$ , was pipetted onto an agarose substrate and allowed to gel under saturated atmosphere (humidity 100%) within an incubator. The shapes of the two samples were photographed with a Drop Shape Analyzer (DSA30, KRUSS) at an angle of 2° with respect to the deposition surface.

#### *Turbidity*

*In-situ* turbidity measurements were conducted as follows. The beam of a continuous wave argon-ion laser ( $\lambda=488\text{nm}$ , 200mW, Spectra-Physics) was expanded ten times, guided with a mirror to vertically penetrate an optically clear measurement section and collected by an amplified photodetector (Thorlabs). Sheet deposition experiments were conducted on top of the measurement section, within an agarose coated petri dish. The absorbance of the petri dish and the agarose was found to small in comparison with the

time-changing absorbance of the bioink layer. The handheld Skin Printer was used to deposit sheets of fibrin-HA bioink with different thicknesses (100, 200, 400, and 600  $\mu\text{m}$ ) on top of the agarose layer at a deposition speed of  $V=4\text{mm/s}$ . The voltage signal ( $U$ ) generated from the transmitted laser light was acquired using an oscilloscope (Tektronix). To quantify the *in-situ* turbidity (IST), the voltage signal,  $U(t)$ , recorded by the oscilloscope was converted to absorbance by  $A(t) = -\log(U(t)/U_0) = \alpha\delta$  where  $U_0$  is the voltage read by the oscilloscope in the absence of a sheet,  $\alpha$  is the absorption coefficient ( $\text{cm}^{-1}$ ),  $\delta$  is the sheet thickness. The turbidity,  $\tau(t) = \left(\frac{A(t)}{\delta}\right) \ln 10$ , was plotted for times  $t > 3\text{s}$ , after the microfluidic cartridge had obstructed the light path.

### ***Stripe and Spot Size***

Two bioink syringes were prepared and loaded onto the handheld Skin Printer. The secondary bioink solution contained fluorescent Nile red microparticles (FCM-1056-2, Spherotech). The primary bioink contained no particles. The cross-linker solution was supplied with an external syringe pump (PHD 2000, Harvard Apparatus). Stripe patterned sheets were deposited using a dedicated microfluidic cartridge design. Its microchannel configuration allowed the formation of biopolymeric sheets where stripes or spots of the secondary bioink were periodically incorporated within the primary one. Varying the flow rate ratio of the secondary and primary bioinks allowed the relative stripe widths to be controllably varied. Upon gelation, stripe-patterned sheets were transferred onto cover slides for confocal microscopy. The reported stripe width represents an ensemble average over the individual stripe widths measured at 3 points (top, middle, bottom), over all stripes. ImageJ was used for image analysis.

In sheets with incorporated spotted patterns, another microfluidic cartridge design was used. The secondary bioink was supplied from an on-chip reservoir (i.e., instead of a syringe pump). After priming the reservoir with the fluorescently labelled secondary bioink, a square-wave pressure signal was applied to the air-filled headspace. Spot size and volume were controlled by adjusting the upper pressure level, and the valve open times. A solenoid valve (LHL series, Lee Company) controlled with an Arduino Mega microcontroller allowed to change the frequency and the duty cycle of the pressure signal.

### ***Tensile Properties***

Uniaxial tensile measurements of the collagen and agarose sheets were measured using a custom instrument based on the ones described by Tremblay *et al.*<sup>1</sup> The hydrated and approximately 10 mm long sample sheets were on two opposing sides attached to custom C-shaped clamps using sand paper. Clamps were positioned in the vertical direction,  $z$ , using manual translation stages (MT1B; Thorlabs). Motion along the direction of pulling,  $x$ , was controlled by a linear voice coil motor (LVCM-051-051-01, MotiCont) on a ball bearing slide (37-360, Edmund Optics). A motion controller (DMC-4143, Galil) was addressed using a custom LabVIEW software program and controlled the displacement of the voice coil motors in feedback mode with an optical encoder (MII 1610S-40, Celera Motion) signal. Samples were pulled at a speed of 0.01 mm/s and displaced until fracture. A load cell (Model 31 Low, Honeywell) measured the force at a given displacement. A DAQ Card (USB-1208LS, Measurement Computing) and amplifier (Model UV-10, Honeywell) were used to transfer the signal from the load cell to the motion controller.

Sample length and width were evaluated using Zeiss and Nikon Ti inverted microscopes, to calculate the cross-sectional area. The cross-sectional area in combination with the motor position and the load-cell corrected force resulted in a stress-strain curve. A linear regression was fitted to the elastic region to calculate the Young's modulus of each sample.

### ***Microstructure Analysis***

Alginate, collagen, and fibrin based biomaterials were fixated for one hour with Karnovsky's style fixative in Sorensen's buffer at room temperature, then dehydrated in serial ethanol washes with solutions containing between 30% and 100% ethanol. Samples were then dried using a critical point dryer. Gold was sputtered, prior to imaging on a scanning electron microscope (S-3400N, Hitachi) using an accelerating voltage of 30 kV.

### ***Cell Sources***

Human dermal fibroblasts (HDFa) were obtained from healthy human normal skin after surgery. Cells were cultured in growth medium (DMEM, 10% fetal bovine serum (FBS) and 1% antibiotic/antimycotic (Ab/Am) until near confluency and split into further passages by treatment with 0.05% trypsin-EDTA treatment. Human Epidermal Keratinocytes, neonatal (HEKn: C-001-5C, Gibco Invitrogen) were cultured according to company instructions in EpiLife Medium with 1% HKGS and 1% Ab/Am and trypsinized using the same trypsin-EDTA solution as for fibroblasts. Cell passages 3-5 were used throughout this study.

### ***Deposition of Cell-Populated Sheets***

For *in vitro* preparation of cell-laden sheets, the dermal bioink contained  $0.5 \times 10^6$  human primary fibroblasts per ml and was deposited as a  $\delta_D = 500 \mu\text{m}$  thickness sheet on agarose. The sheet was incubated at  $37^\circ\text{C}$  for 20 min to allow for complete thermal gelation of collagen. The epidermal bioink contained  $1.5 \times 10^6$  human primary keratinocytes per ml. The epidermal layer was printed sequentially on top of the dermal layer with a thickness  $\delta_E = 200 \mu\text{m}$ . Depending on the study, different patterns of epidermal layer (homogeneous or striped) were deposited on top of the dermal layer. The sheets were then immersed in culture media (EpiLife Medium, with  $60 \mu\text{M}$  calcium, Gibco<sup>TM</sup>). Sheets were then detached from the agarose substrate, sectioned to desired sizes and cultured in multiwell plates.

### ***Cell Viability***

Human dermal fibroblasts and keratinocytes were cultured in collagen/fibrin and fibrin gels, respectively, for three days in EpiLife media with HKGS growth supplement and 1% penicillin-streptomycin. Cells were then stained using calcein and ethidium homodimer for analysis of live versus dead cells, in addition to Hoechst as a cell nucleus stain. Confocal images of cells in biomaterials in individual 96-well plates were taken at  $4\times$  and  $10\times$  scanning objective with three biological replicates. The ImageJ software was used to determine the percentage of viable cells by counting the number of cells stained positive for either calcein or ethidium homodimer in comparison with the total number of cells as indicated using Hoechst nuclear stain.

### ***Cell Density***

Human dermal fibroblasts and keratinocytes were cultured for three days using the previously described method.<sup>2</sup> Cell density was observed by staining the cells with Hoechst, imaging with confocal microscopy, and calculating the total number of cells using the ImageJ software.

### ***Immunohistochemistry***

Cells in sheets were fixed with 4% paraformaldehyde in HBSS for 1 h at room temperature then washed with HBSS. They were permeabilized with 0.5% Triton X-100 in HBSS for 30 min at room temperature and then washed with HBSS. Cells were blocked with blocking buffer (1% BSA in 0.25% Triton X-100 in HBSS) for 1 h. Antibodies were diluted in block buffer and incubated overnight at 4°C. Primary antibodies included fluorescein phalloidin (Life Technologies) and cytokeratin 14 (Santa Cruz Biotechnology). In cases where only phalloidin staining was performed, the mounting step was performed next. With keratinocytes, samples were washed with HBSS then incubated with secondary Alexa Fluor antibodies (Life Technologies). After 3 washes, slides were mounted with Vectashield mounting medium with DAPI (Vector Laboratories). Images were taken on Apotome Axiovert whole field fluorescence or Observer Z1 spinning disk confocal microscope (both Zeiss).

### ***Histology***

Tissue specimens were fixed in 10% buffered formalin overnight at 4°C, stored in 70% ethanol and embedded in paraffin. Specimens were cut into 5 µm sections in the centre of the wound. Trichrome reagents were obtained from EMS (Hatfield) unless otherwise stated. Briefly, paraffin embedded slides were deparaffinized with citrosol, followed by rehydration through grades of ethanol to water. Slides were placed in Bouin's solution for 1 h at 60°C and washed in water. Hematoxylin (Sigma) and Biebrich scarlet-acid fuchsin solution were stained for 10 min each, respectively with washes in between. Slides were differentiated in phosphomolybdic-tungstic acid for 15 min, and transferred to aniline blue for 5 min. Slides were rinsed and differentiated in 1% acetic acid for 2 min. Slides were dehydrated through 95% ethanol and absolute ethanol followed by clearing in citrosol. Slides were mounted with SHUR/Mount xylene-based liquid mounting medium (Triangle Biomedical Sciences). Images were acquired using a light microscope (Leica DM 2000LED).

For immunohistochemistry staining, paraffin embedded skin tissue slides were deparaffinized with citrosol followed by rehydration. Antigen decloaker (1X, Biocare) was added to the slides in a preheated decloaking chamber for 4 min at 110°C. Samples were blocked with 3% H<sub>2</sub>O<sub>2</sub> for 10 min, then washed with washing buffer (0.05 M Tris-HCl, 0.15 M NaCl, 0.05% Tween 20 in DI water). Primary antibody was diluted in PBS and incubated at room temperature for 1 h. Next, slides were incubated for 15 min first with goat-on-rodent probe (Biocare Medical), and secondly with goat-on-rodent HRP-polymer. The betazoid DAB chromogen kit (Biocare Medical) was added for 5-10 min and the reaction was terminated with running water. Nuclear staining was done with hematoxylin for 30 s, followed by differentiation with 3 dips in 1.5% acid alcohol and bluing in 0.1% sodium bicarbonate for 10 s. Sections were dehydrated through 95% and

absolute ethanol to citrosol and mounted with SHUR/Mount as previously described. Images were acquired using LeicaDM 2000LED light microscope.

### ***In Vivo Deposition Using Porcine Model***

A male Yorkshire pig with a weight of 25 kg was exposed to excisional skin biopsy following the reviewed protocol by Sunnybrook animal care committee (AUP #: 17-600). The pig was housed in individual pens at room temperature and at a 12 h light-dark cycle with food and water ad libitum at Sunnybrook Research Institute. Feeding and daily care was performed by the in-house animal staff and overseen by an assigned veterinarian. Standard diet and animal care standard operation procedures were obeyed. All animals were fasted for at least 6 h before surgery and assessed daily using a standardized protocol elaborated together with the veterinarian. Pain medication was adjusted accordingly. After induction of anesthesia, hair was removed via electrical shaving followed by chemical depilation. The operation area was disinfected with povidone Iodine, skin excision in the previously marked areas was performed with a scalpel, the rest of the operation with a monopolar diathermy knife that was also used for hemostasis.

Both treated wounds and control wounds dressed with the following layers: Jelonet® paraffin gauze, Polysporin® cream, wet gauze, dry gauze, Tegaderm® transparent film dressing, gauze rolls, and a lamb-tube compression jacket. Dressing changes and wound evaluations were done every 3 days under general anesthesia and sterile conditions. At the end of the experiment after 20 days, the swine was euthanized, and the wounds/scars were excised, fixed in formaldehyde and send for histological preparation. All tissue for staining was embedded in paraffin, cut into 5µm thick slices and placed on standard glass slides for trichrome staining and immunohistochemical staining. For staining, after deparaffinization with citrosol (CitriSolv Hybrid™, Decon Labs), the tissue containing slides were incubated in Bouin's solution (Bouin's Fixative, Electron Microscopy Sciences) for 24 h at room temperature. Staining was done as follows: hematoxylin (Harris Hematoxylin Solution, Sigma-Aldrich), Bibrich Scarlet Acid Fuchsin (Electron Microscopy Sciences), followed by aniline blue (Electron Microscopy Sciences).

### ***In Vivo Deposition Using Murine Model***

3 male NOD.Cg-Prkdc<sup>scid</sup> Il2rg<sup>tm1Wjl</sup>/SzJ (Jackson Laboratory) at 1 year old were used for in the *in-situ* pattern formation experiments following the reviewed protocol by Sunnybrook animal care committee (AUP #: 17-503). Mice were anesthetized with isofluorance. One 1 cm × 2 cm or two 8 mm diameter full thickness wounds were inflicted on the back of the mouse. The handheld instrument was used to deposit architected sheets while mice were under anesthesia. A 8 mm wide microfluidic cartridge was manually translated at a speed of approximately 2 mm/s for *in situ* delivery of 4 parallel stripe filaments or stripe-patterned sheets. The wounds were illuminated by the ultraviolet light that passed through a 405 nm bandpass filter (model FB405-10, Thorlabs) from a high-pressure mercury lamp (model C-SHG1, Nikon). The reflected light was collected at 488 nm (FL488-1, Thorlabs). Images were captured using a DSLR camera (Nikon D500) at a high ISO setting. Mice were euthanized using cervical dislocation after completion of the experiment, approximately 30 min after the mouse

underwent anesthesia. ImageJ was used to evaluate the light intensity distribution across the width of the sheet.

Bioink	Main Biopolymer	Secondary Biopolymer	pH	Media	Viscosity (at 1 s <sup>-1</sup> shear rate)	Crosslinker	Gelation rate
Polysaccharide based	Alginate 2% (w/v)	-	7	DMEM + 20mM HEPES	80 mPa·s	50 mM Calcium Chloride in PBS	200 μm/min
	Alginate 2% (w/v)	Collagen type 1 (2.5 mg/ml)	7 (modified with NaOH)	DMEM + 20mM HEPES	108 mPa·s	50 mM Calcium Chloride in PBS	200 μm/min, 10-30 min thermal gelation
Protein based	Fibrinogen (20 mg/ml)	Hyaluronic acid 0.5% (w/v)	7	PBS or DMEM	1.18 Pa·s	50 IU Thrombin in PBS	Fig 2e
	Fibrinogen (20 mg/ml)	Hyaluronic acid 0.5%, collagen type 1 (2.5 mg/ml)	7 (modified with NaOH)	PBS or DMEM	0.95 Pa·s	50 IU Thrombin in PBS	Fig 2e, 10-30 min thermal gelation

**Table S1** Formulation of bioink and cross-linker combinations used in present work.

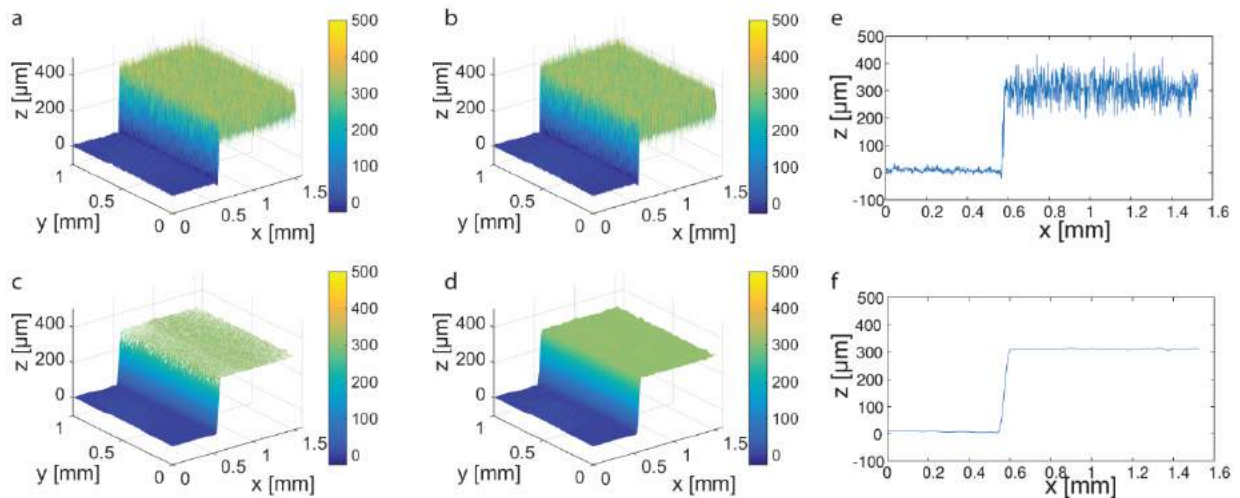


**Figure S1.** Representative sheet thickness measurement data showing edge of 300 μm thick fibrin/HA sheet deposited onto agarose substrates, as obtained from optical profilometry. (a) Sheet thickness raw data as obtained from profilometer. (b) Filled data with averaging the NaN values over 4-data-point radius. (c) Smoothed raw data using MatLab smoothing splines built-in function. (d) Filled and smoothed data used for in reported sheet thicknesses. (e) Cross-sectional view of sheet thickness at edge of *in-situ* deposited sheet. (f) Cross-sectional view of sheet thickness at edge of *in-situ* deposited sheet.

## S2. Design and Assembly of Handheld Skin Printer

The handheld Skin Printer is designed to meet the requirements of biocompatibility, portability and light weight, and robustness to small changes in position during handheld operation. The instrument has a modular design where individual modules are attached to a common base plate. They are two syringe pump modules for bio-ink and cross-linker delivery, a module for controlling the bioink temperature, a roller drive module for controlling the speed of sheet deposition, and a microfluidic cartridge defining the width and composition of the deposited sheets. The modules are described in detail below.

### *Syringe Pump Module*

The handheld Skin Printer contains two independently controlled 3D printed syringe pump modules that can accommodate individual 3ml (model 309657, BD) syringes. The syringe pump is shown in **Figure S2**. and based on a lead screw and nut design, similar to the one employed in standard commercial syringe pumps.

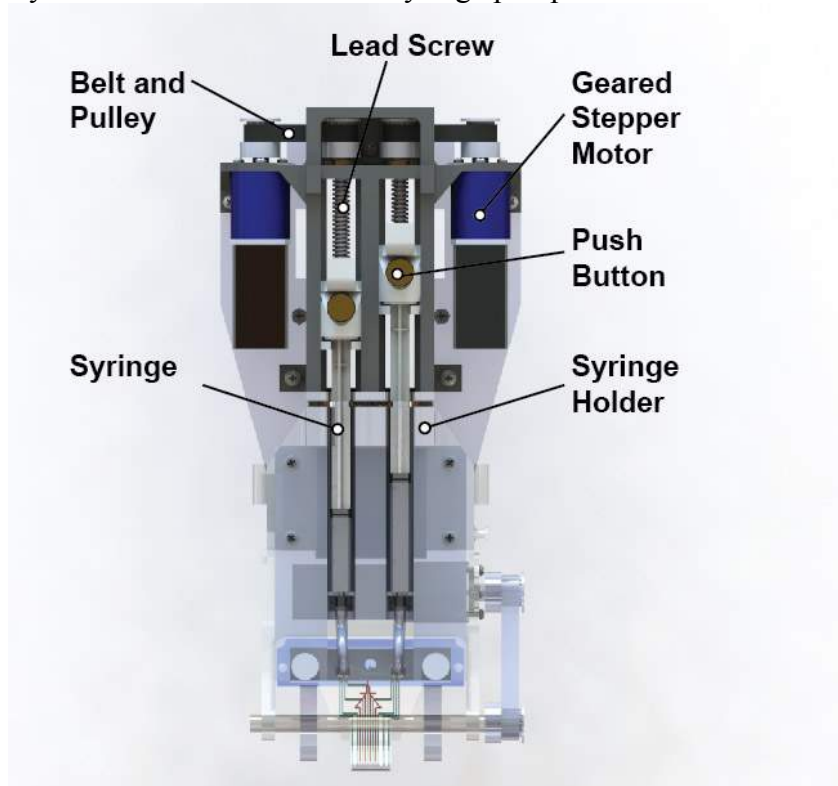


**Figure S2.** Two syringe pump modules are secured to Skin Printer base plate. Rotation of stepper motors (Nema 8, 1:19 gear ratio) is transferred to lead screws via belt-and-pulley system. Speed of stepper motors rotation is controlled externally via a control box. Adjustable push buttons are custom machined and allow to load or exchange 3ml syringes. Syringe pump modules provide smooth and consistent delivery of bioink and cross-linker solutions at desirable volumetric flow rates irrespective of their viscosities.

For each module, the rotational motion from a Nema 8 (gear ratio 19:1, model 8HS15-0604S-PG19, Stepper Online) geared bi polar stepper motor is transferred to the lead screw via a belt-and-pulley system (part numbers 7887k7 and 1375k35, McMaster-Carr). ACME size  $\frac{1}{4}$ " – 16 lead screws turn inside a block containing a spring-loaded half nut

that is in dispensing mode engaged with the lead screw to provide a direct-drive connection. Pressing a custom-machined button temporarily disengages the half nut from the lead screw, e.g., to load or exchange a bioink or cross-linker syringe. The linear motion of the block translates the syringe plunger and controllably dispenses the solution from the syringe. A digital stepper driver (model DM422C, Stepper Online) in combination with a (Arduino model Due) allows to select the flow rate for each pump module.

### ***Roller Drive Module***

The movement system of the Skin Printer is shown in **Fig. S3** and composed of a timing belt-and-pulley system powered by a geared stepper motor (Nema 8, 1:19 gear ratio). The motor is placed under the block accommodating the two syringe barrels. The rotational movement is conveyed via a stainless-steel shaft (part 1327k66, McMaster-Carr) to two elastomeric roller wheels (wheel diameter 25.4mm, wheel width: 6.4mm, shore hardness: 70A, part 2488K44, McMaster-Carr) that engage with the deposition surface to control the deposition velocity,  $V$ . The latter in combination with the flow rates provided by syringe pump modules control the thickness of the deposited biopolymer or tissue sheet.

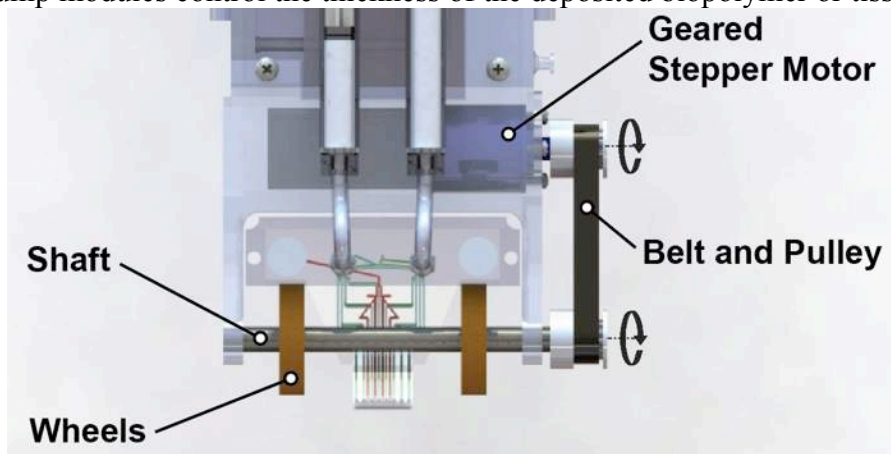


**Figure S3. Roller drive module.** Two elastomeric roller wheels are located at each side of the microfluidic cartridge. The wheels engage with the deposition surface, and are connected via a shaft that is rotated via a belt-and-pulley system. By adjusting the roller speed, the instrument is translated over the deposition surface at the deposition velocity  $V$ .

### ***Pressure Controller Module***

Filtered air at a constant pressure is provided externally via a digital pressure controller (3411, March Bellofarm). A solenoid valve periodically selects between this pressure and ambient pressure and thereby applies a square-wave pressure signal at the head of a well containing the secondary bioink. Duty cycle and frequency of the pressure signal are adjusted via a solenoid valve (LHL series, Lee Company) controlled by Arduino Mega.

### ***Microfluidic Cartridge Fabrication and Cleaning***

The microfluidic cartridge is a crucial part to the handheld instrument. Dedicated designs were prepared for 8 mm, 14 mm and 21 mm wide sheets. Stereolithography (STL) design files were prepared using a computer aided design program (Solidworks 2015, Dassault

Systems). The parts were printed using a 3D printer (model ProJet 3510 SD, Ultra High-Resolution option, 3D Systems) using the resin VisiJet M3 Crystal (3D Systems). Up to 20 cartridges were usually printed simultaneously. The support material was removed by sonication in mineral oil (O122-1, Fisher Scientific) at 65 °C for 1 h. Microchannels were cleaned by perfusion of hot mineral oil with a syringe, and subsequent slow cooling to room temperature. Cartridges were then kept in 70% ethanol overnight. Prior to use, cartridges were sterilized by perfusion of 70% ethanol for 30 min and subsequent perfusion of phosphate-buffered saline (PBS) for 5 min. In the following section, we discuss the components of the microfluidic cartridge.

### ***Microfluidic Cartridge Design***

3D printing allowed us to integrate world-to-chip fluidic interfaces without the use of any external tubing or manifolds. In our handheld Skin Printer, the feed lines from syringes or a pressure controller are directly connected to 3D printed Luer lock connectors on the microfluidic cartridge. As a result, the microfluidic cartridge has a very low dead-volume of ~ 25 -90  $\mu\text{L}$ , depending on the width of the cartridge width, and can withstand pressures as high as 60 psi without leakage or failure.

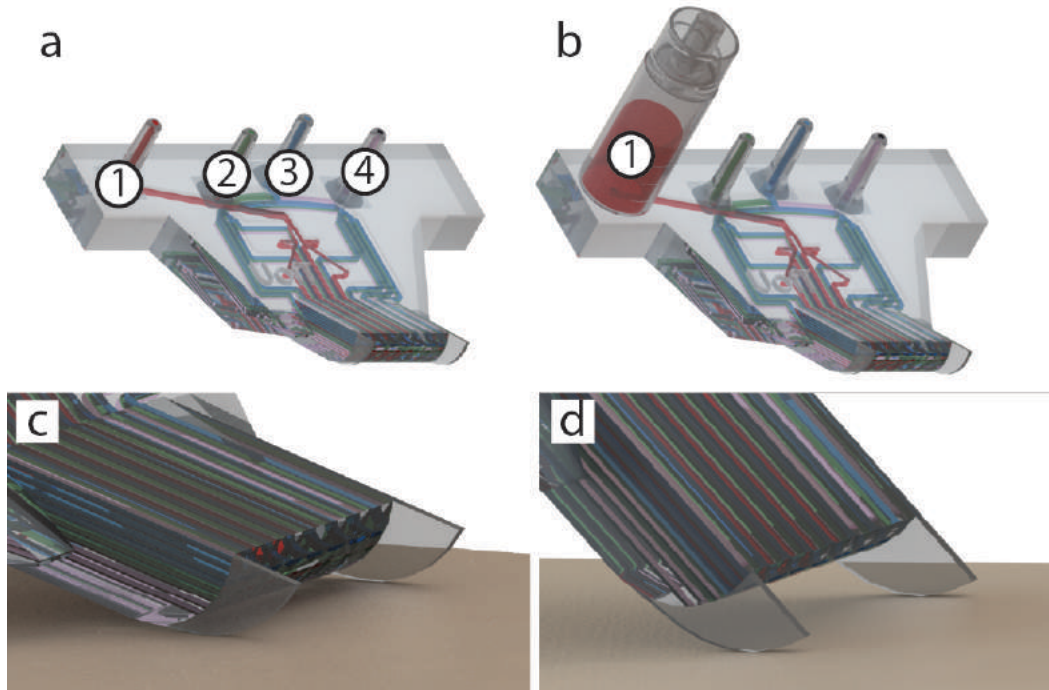


**Figure S4. Microfluidic Cartridge.** (a) Rendered image of microfluidic cartridge for deposition of 14 mm-wide sheets. Flow rates at all inlets are controlled by syringe pumps. Numbers are indicating the following designated inlets for ① secondary bioink for architected sheets, ② primary bioink for architected sheets, ③ cross-linker, and ④ primary bioink for homogenous sheets. (b) Rendered image of microfluidic cartridge for deposition of 14 mm-wide sheet. Inlet for secondary bioink contains fluid reservoir for head-pressure controlled delivery. (c) and (d) Enclosed views of guidance features maintaining gap height  $H \sim 1$  mm between device exit and deposition surface for two different operator-selected deposition angles.

The 3D printed cartridges allowed us to readily accommodate multi-layered flow distribution networks, without increasing fabrication cost. The bioink passes through a hierarchical network located close to the bottom of the cartridge and delivers at the exit a uniform thickness bioink layer. Above it, a separate hierarchical microchannel network distributes the cross-linking fluid and delivers it on top of the bioink layer, inducing gelation in the bioink.

3D printing allowed us to incorporate out-of-plane features in the microfluidic cartridge at no fabrication penalty. As shown in **Figure S4**, the layered fluids exited the microfluidic cartridge at a narrow angle with respect to the deposition surface. Two circular arc-shaped guiding features at the tip of the microfluidic cartridge allowed us to maintain a consistent distance between the cartridge tip and the deposition surface, even if the angle varied. These features greatly improved consistency of the deposition during manual operation of the handheld instrument. Reproducible fabrication of these features was readily achieved using the selected 3D printing process.

Murray's law<sup>3</sup> describes the relationship between the sizes of the daughter branches in a hierarchical flow network compared with the sizes of the parent branch. The diameter of the parent branch is related to the diameters of the (1...*n*) daughter branches as follows:  $d_p^3 = d_1^3 + d_2^3 + d_3^3 + \dots + d_n^3$ . The law is being used widely as a biomimetic design criterion for hierarchical flow networks. Applying Murray's law in the design of microfluidic channel networks ensures that the wall shear stress in the daughter branches is equal to the one in the parent branch. As a result, the flow distribution is significantly more uniform compared with a microfluidic device with constant hydraulic diameter throughout all branches. Emerson *et al.*<sup>4</sup> have discussed the application of Murray's law for improving the flow distribution in hierarchical networks of microchannels with rectangular cross-section. Microchannel networks defined using planar, lithography-based processes, often are required to have rectangular cross sections with a uniform depth. 3D printing however allows realizing arbitrary cross-sectional shapes where both the channel width and depth are varied, a distinct advantage in the design of hierarchical microchannel networks (**Fig. 5Sa**) over traditional lithography-based approaches.

For the preparation of stripe-patterned sheets a primary and a secondary bioink are introduced to separate device inlets and passed through separate hierarchical microchannel networks. Close to exit of the cartridge, the smallest daughter channels of these two channel networks are arranged in the flow focusing configurations shown in **Fig. S5b**. This configuration allows stripes of the secondary bioink to be incorporated within sheets of the primary one at a stripe width that is smaller than the width of the smallest daughter channels. The representative channel geometry shown in Fig. S5 was used for achieving the stripes in **Fig. 4b**.

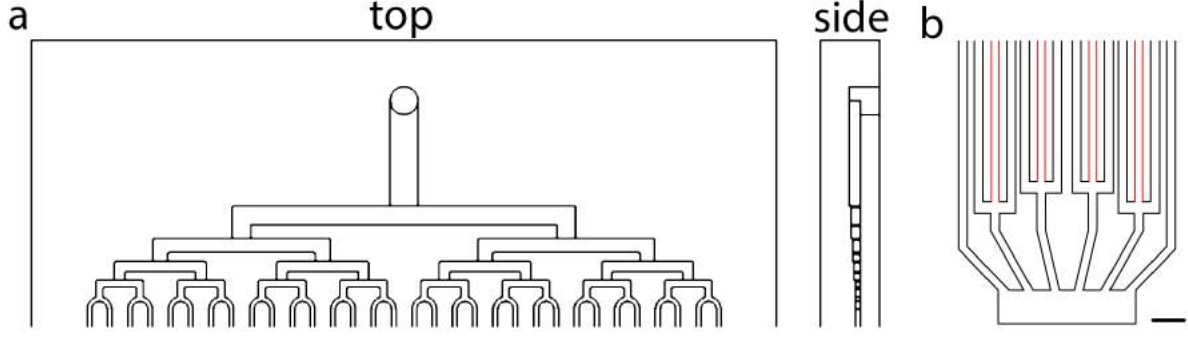


**Figure S5.** (a) Representative microchannel network in one layer of the microfluidic cartridge. The hydraulic diameters of parent and daughter channels satisfy the Murray law. (b) Representative channel geometry for producing four stripe sections of a secondary bioink. Walls of the channels carrying the secondary bioink are depicted in red color. Scale bar 1.5 mm.

### S3. Analytical Model for Biopolymer Sheet Deposition

Laminar flow of a viscous fluid through a narrow gap  $H$  between two horizontal plates ( $w/H > 10$ ) is well described by lubrication theory<sup>5</sup> where the hydraulic diameter is then approximately equal to  $2H$ . With the lubrication approximations we write for the bioink flow (subscript “M”):

$$\frac{\partial p}{\partial x} z = \mu_M \frac{\partial^2 u}{\partial z^2}$$

and or the cross-linker flow (subscript “C”):

$$\frac{\partial p}{\partial x} z = \mu_C \frac{\partial^2 v}{\partial z^2}.$$

The velocity profiles have the general solution for the bioink flow  $u = -\frac{a_2 + a_1 z + \frac{\partial p}{\partial x} z^2}{\mu_M}$ , and for cross-linker flow  $v = -\frac{b_2 + b_1 z + \frac{\partial p}{\partial x} z^2}{\mu_C}$ .

The boundary condition for the velocity at the bottom surface is  $u(z = 0) = V$ , and the velocity at the top surface is  $u(z = H) = 0$ . The shear stress is required to be the same at the interface between the bioink and cross-linker layers  $\mu_M \frac{du}{dz} \Big|_{z=\delta} = \mu_C \frac{dv}{dz} \Big|_{z=\delta}$ .

Solving for  $a_1, a_2, b_1, b_2$ , and substitution gives the velocity distribution within the bioink layer:

$$u = -\frac{((\delta - H)\mu_M^2 - \delta\mu_M\mu_C)V + \left(\mu_M\mu_C V + ((\delta^2 - H^2)\mu_M - \delta^2\mu_C) \frac{\partial p}{\partial x}\right) z + (\delta\mu_C + (H - \delta)\mu_M) \frac{\partial p}{\partial x} z^2}{\delta\mu_M\mu_C + (H - \delta)\mu_M^2}.$$

Similarly, we obtained for the velocity distribution within the cross-linking solution:

$$u = - \frac{((\delta^2 H - \delta H^2)(\mu_C + \mu_M)) \frac{\partial p}{\partial x} - H \mu_M \mu_C V + \left( \mu_M \mu_C V + ((\delta^2 - H^2) \mu_M - \delta^2 \mu_C) \frac{\partial p}{\partial x} \right) z + (\delta \mu_C + (H - \delta) \mu_M) \frac{\partial p}{\partial x} z^2}{\delta \mu_C^2 + (H - \delta) \mu_M \mu_C}.$$

We express the dimensionless velocity,  $u^* = \frac{u}{V}$ , as function of the dimensionless length scales  $z^* = \frac{z}{H}$  and  $\delta^* = \frac{\delta}{H}$ , a dimensionless pressure gradient,  $\Pi = \frac{H^2 \frac{\partial p}{\partial x}}{\mu_C V}$ , and a viscosity ratio,  $\mu^* = \frac{\mu_C}{\mu_M}$ . We obtain for the bioink layer

$$u^* = \frac{-1 + \delta^* - \delta^* \mu^* + \left( ((\delta^{*2} - 1) \mu^* - \delta^{*2} \mu^{*2}) \Pi + \mu^* \right) z^* + (\delta^* \mu^{*2} + (1 - \delta^*) \mu^*) \Pi \epsilon z^{*2}}{\delta^* \mu^* - \delta^* + 1}$$

and for the cross-linker layer

$$u^* = \frac{-1 + \left( (\delta^{*2} - \delta^*) \mu^* - \delta^{*2} + \delta^* \right) \Pi + \left( (-1 + \delta^{*2} - \delta^{*2} \mu^*) \Pi + 1 \right) z^* + (\delta^* \mu^* - \delta^* + 1) z^{*2}}{\delta^* \mu^* - \delta^* + 1}$$

Replacing volumetric flow rate of each layer by integration in the  $z$  direction

$$Q_M^* = \frac{Q_M}{w_0 V H} = \int_0^{\delta^*} \frac{-1 + \delta^* - \delta^* \mu^* + \left( ((\delta^{*2} - 1) \mu^* - \delta^{*2} \mu^{*2}) \Pi + \mu^* \right) z^* + (\delta^* \mu^{*2} + (1 - \delta^*) \mu^*) \Pi z^{*2}}{\delta^* \mu^* - \delta^* + 1} dz^* = \frac{6\delta^* - 6\delta^{*2} + 3\delta^{*2} \mu^* + (\delta^{*4} \mu^{*2} + (3\delta^{*2} - 2\delta^{*3} - \delta^{*4}) \mu^*) \Pi}{6\delta^* \mu^* - 6\delta^* + 6},$$

and solving for the dimensionless pressure gradient leads to

$$\Pi = \frac{-6\delta^* + 6\delta^{*2} - 3\delta^{*2} \mu^* + (6\delta^* \mu^* - 6\delta^* + 6) Q_M^*}{\delta^{*4} \mu^{*2} + (3\delta^{*2} - 2\delta^{*3} - \delta^{*4}) \mu^*}.$$

Similarly, for the dimensionless cross-linker flow rate we obtain

$$Q_C^* = \frac{Q_C}{w_0 V H} = \int_{\delta^*}^1 \frac{-1 + \left( (\delta^{*2} - \delta^*) \mu^* - \delta^{*2} + \delta^* \right) \Pi + \left( (-1 + \delta^{*2} - \delta^{*2} \mu^*) \Pi + 1 \right) z^* + (\delta^* \mu^* - \delta^* + 1) z^{*2}}{\delta^* \mu^* - \delta^* + 1} dz^* = \frac{-3 + 6\delta^* - 3\delta^{*2} + \left( (-4\delta^* + 9\delta^{*2} - 6\delta^{*3} + \delta^{*4}) \mu^* - \delta^{*4} + 4\delta^{*3} - 6\delta^{*2} + 4\delta^* - 1 \right) \Pi}{6\delta^* \mu^* - 6\delta^* + 6}.$$

Substitution of  $\Pi$  gives

$$\begin{aligned}
&(\mu^* - 1)\delta^{*5} + (4 - 4\mu^* + (1 - \mu^*)Q_M^* + (\mu^* - \mu^{*2})Q_C^*)\delta^{*4} + (-6 + 5\mu^* + \\
&(6\mu^* - 4)Q_M^* + 2\mu^*Q_C^*)\delta^{*3} + (4 - 2\mu^* + (6 - 9\mu^*)Q_M^* - 3\mu^*Q_C^*)\delta^{*2} + \\
&((4\mu^* - 4)Q_M^* - 1)\delta^* + Q_M^* = 0.
\end{aligned}
\tag{S1}$$

For  $\mu_M = \mu_C, \mu^* = 1$ , the 5<sup>th</sup> order polynomial in **Equation (S1)** reduces to 3<sup>rd</sup> order with solutions in the form  $\delta^* = f(\mu^*, Q_M^*, Q_C^*)$ . Only one solution has a real value between 0 and 1. Substituting the obtained  $\delta^*$  leads to

$$\Pi = \frac{-6\delta^* + 6\delta^{*2} - 3\delta^{*2}\mu^* + (6\delta^*\mu^* - 6\delta^* + 6)Q_M^*}{\delta^{*4}\mu^{*2} + (3\delta^{*2} - 2\delta^{*3} - \delta^{*4})\mu^*}.$$

The dimensionless velocity profile in each layer can be calculated by substituting  $\delta^*$  and  $\Pi$ :

$$\begin{aligned}
u^* &= \frac{-1 + \delta^* - \delta^*\mu^* + \left( \left( (\delta^{*2} - 1)\mu^* - \delta^{*2}\mu^{*2} \right) \Pi + \mu^* \right) z^* + (\delta^*\mu^{*2} + (1 - \delta^*)\mu^*) \Pi z^{*2}}{\delta^*\mu^* - \delta^* + 1} \quad \text{for } 0 < z^* < \delta^* \text{ and} \\
u^* &= \frac{-1 + \left( (\delta^{*2} - \delta^*)\mu^* - \delta^{*2} + \delta^* \right) \Pi + \left( (-1 + \delta^{*2} - \delta^{*2}\mu^*) \Pi + 1 \right) z^* + (\delta^*\mu^* - \delta^* + 1) z^{*2}}{\delta^*\mu^* - \delta^* + 1} \quad \text{for } \delta^* < z^* < 1.
\end{aligned}$$

**Equation S1** is solved numerically using a built-in root finder function in Matlab. **Table S2** summarizes the experimental conditions.

**Table S2. Selected experimental conditions.**

Property	Symbol	Range of Values	Units
Confinement height	$H$	1-2	mm
Confinement length	$L$	1-20	mm
Device width	$w_0$	10-60	mm
Deposition velocity	$V$	0.5-10	mm/s
Volumetric flow rate of cross-linking solution	$Q_C$	150 - 1000	$\mu\text{L}/\text{min}$
Volumetric flow rate of bioink	$Q_M$	150 - 1000	$\mu\text{L}/\text{min}$
Viscosity of cross-linking solution	$\mu_C$	1-100	cP
Viscosity of bioink	$\mu_M$	70-1150	cP

The values selected for the non-dimensional parameters were on the order of the ones reported in **Table S3**.

**Table S3. Corresponding dimensionless conditions.**

Dimensionless Quantity	Expression	Value
$Q_C^*$	$\frac{Q_C}{wVH}$	0.55
$Q_M^*$	$\frac{Q_M}{wVH}$	0.55
$\mu^*$	$\frac{\mu_C}{\mu_M}$	0.01

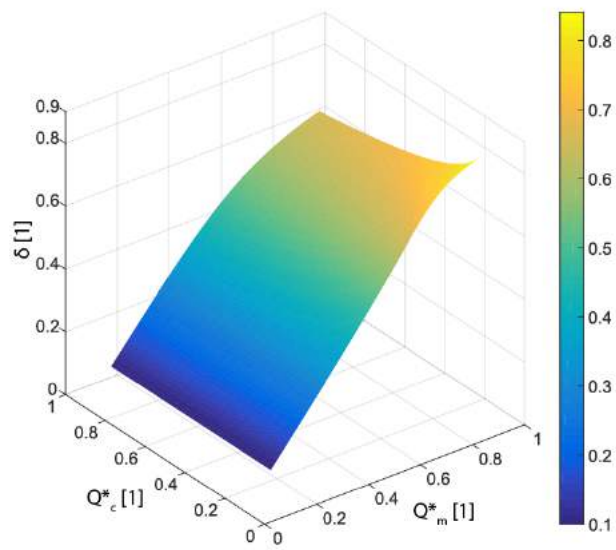


**Figure S6.** Analytically predicted sheet thickness as a function of both  $Q_C^*$  and  $Q_M^*$ , for  $\mu^*=0.01$ .

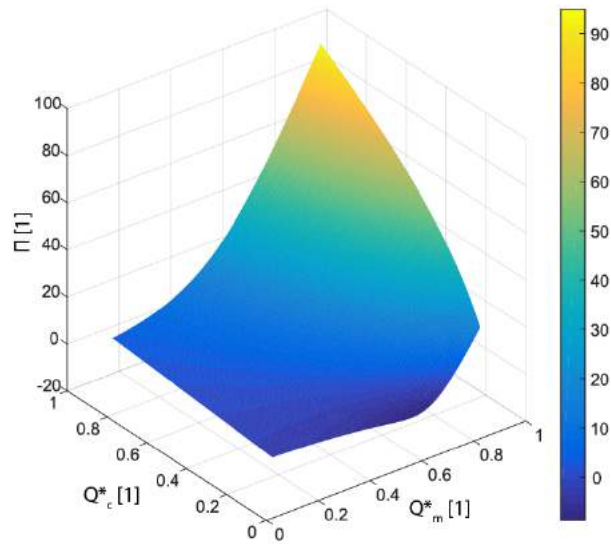


**Figure S7.** Analytically predicted non-dimensional pressure gradient within confinement as function of  $Q_c^*$  and  $Q_M^*$  for  $\mu^*=0.01$ .

For the case of  $P=0$  (zero pressure gradient) and a particular thickness of deposited sheet,  $\delta$ , the equation  $\Pi = 0$  is solved.

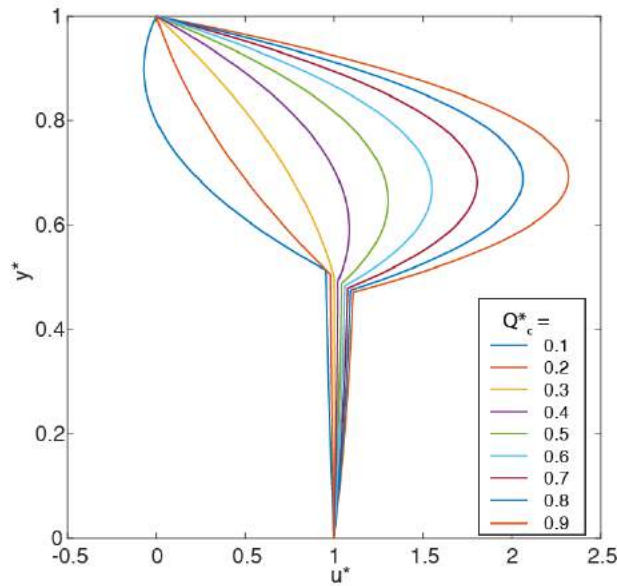


**Figure S8.** Analytical model predicting the effect of  $Q_c^*$  on velocity profile within confinement for special case of  $Q_M^* = 0.5$  and  $\mu^*=0.01$ .

The values for  $Q_c^*$  and  $Q_M^*$  can be obtained accordingly in each case.

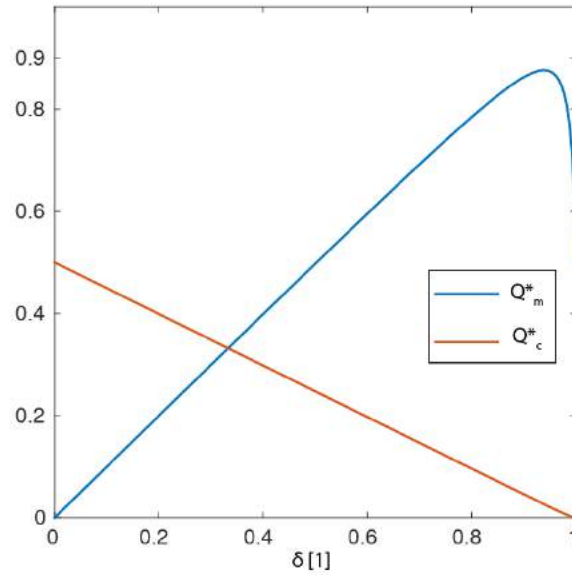


**Figure S9.** Analytical model prediction indicating  $Q_c^*$  and  $Q_M^*$  conditions required for  $\mu^*=0.01$  to meet zero pressure gradient requirement ( $\Pi = 0$ ). Gelation neglected in model.

#### S4. Nominal In-Plane Printing Resolution for Deposition on Inclined Surfaces

The handheld Skin Printer allows for the *in-situ* formation of biopolymeric sheets and tissues *in-vitro* and *in-vivo*. A flat, stiff, and hydrophilic surface (e.g., on an agarose coated petri dish) was selected for sheet deposition *in-vitro*. The rapid gelation that is initiated at the sheet bottom surface as well as along the contact lines at both sides prevents unwanted spreading and thinning of the bioink sheet while gelation progresses to the center of the sheet. During *in-situ* deposition however, inclined and compliant wound surfaces may result in a gravity-induced drainage effect on the deposited sheets prior to gelation being completed. We now discuss the effect of the inclination angle,  $\theta$ , on the nominal resolution of the printed sheets. **Figure S10** shows a schematic illustration.

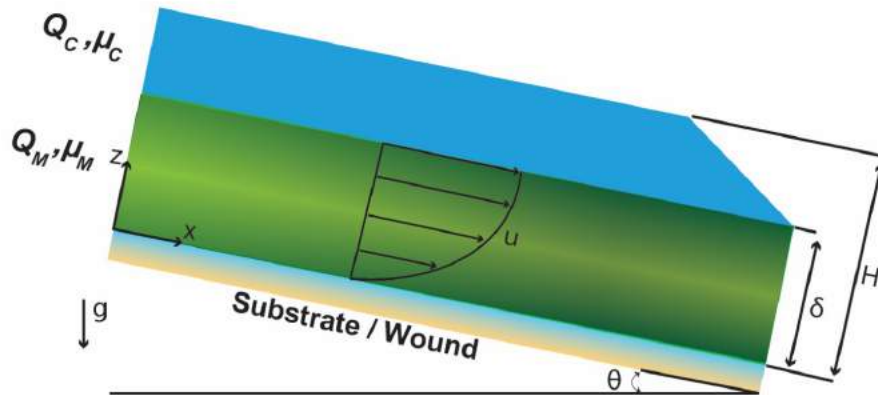


**Figure S10.** Schematic illustration of *in-situ* sheet deposition onto flat surface with inclination angle  $\theta$ .

For the bioink solution, denoted by subscript “M”, we assume steady, incompressible, and fully developed flow. We neglect the viscosity increase due to the gelation (a conservative estimate). The Navier-Stokes equations reduce to:

$$0 = \rho g_x + \mu_M \frac{\partial^2 u}{\partial z^2}$$

$$0 = \rho g_z - \frac{\partial p}{\partial z}.$$

Integrating  $-\frac{\rho g \sin \theta}{\mu_M} = \frac{\partial^2 u}{\partial z^2}$  twice results in

$$u = -\frac{\rho g \sin \theta}{\mu} \frac{z^2}{2} + c_1 z + c_2.$$

Applying a no slip boundary condition at the interface between the bioink and the bottom substrate gives  $c_2 = 0$ . Furthermore we assume  $\mu_M \gg \mu_C$ . At the interface of the two streams,  $z = \delta$ , we obtain  $\frac{du}{dz} = 0$ .

Integration yields the velocity profile  $u = \frac{\rho g \sin \theta}{\mu_M} z(\delta - \frac{z}{2})$ , bioink flow rate  $Q_M = \frac{\rho g \sin \theta w}{\mu_M} \frac{\delta^2}{3}$ , the sheet thickness  $\delta = \left(\frac{3\mu_M Q_M}{\rho g \sin \theta w}\right)^{1/3}$  and  $u_{avg} = \frac{\rho g \sin \theta}{\mu_M} \frac{\delta^2}{3}$  for the average bioink velocity.

The nominal resolution,  $\Delta x$ , is given by the gravitationally induced displacement of the ungelled bioink during a given time interval  $\Delta t$ :

$$u_{avg} = \frac{\Delta x}{\Delta t} = \frac{\rho g \sin \theta}{\mu_M} \frac{\delta^2}{3}$$

$$\Delta t = \frac{3\mu_M}{\rho g \sin \theta \delta^2} \Delta x. \quad (\text{S2})$$

The time scale for gelation,  $t_{gelation}$ , should therefore not exceed  $\Delta t$  in order to achieve the nominal resolution  $\Delta x$ :

$$t_{gelation} < \Delta t.$$

For example, for the fibrin-HA bioink with the measured viscosity  $\mu_M = 1.12 \text{ Pa} \cdot \text{s}$ , an assumed density  $\rho = 1000 \text{ kg/s}$  and the gravitational acceleration  $g = 9.81 \text{ m/s}^2$ . Inflection times of 44 s, 64 s, 110 s and 160s were measured for the respective sheet thicknesses of  $\delta=100 \mu\text{m}$ ,  $200 \mu\text{m}$ ,  $400 \mu\text{m}$  and  $600 \mu\text{m}$  (see **Fig. 2e**). By re-arranging **Equation (S2)** we obtain

$$\Delta x < \frac{\rho g \sin \theta \delta^2}{3\mu_M} t_{gelation}.$$

Here,  $\Delta x$  is an estimate for the bioink movement due to gravitational forces along the target surface, prior to gelation. It can be used as an indication of the printing resolution. In **Fig. 3h** we plotted the above relationship for different sheet thicknesses of fibrin-HA based sheets with respect to the surface inclination angle  $\theta$ .

Alginate fiber filaments may be *in-situ* deposited at a resolution higher than suggested above. Although the gelation time for alginate for the calcium chloride concentration that we used here is approximately 100  $\mu\text{m}/\text{min}$ , the interface of between the bioink and the cross-linker gels much more rapidly, providing a template structure for the not-yet-gelled bioink at the filament center. We hypothesize that this effect helps retaining the geometry during *in-situ* deposition of alginate fiber filaments onto inclined or non-planar surfaces. Examples are the murine wound beds shown in **Fig. S11**.

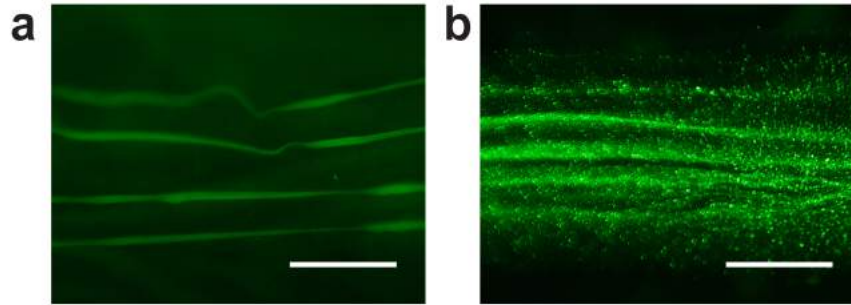


**Figure S11.** Representative fluorescence images of *in-situ* bioprinted of stripe patterned filaments directly into the bed of an excisional murine model. (a) Alginate fiber filaments. (b) Fibrin/HA fiber filaments.

### S5. *In-vitro* Comparison of Total Cell Numbers Before and After Bioprinting

We found, for five different concentrations of cells ranging from 0.1 to 10 million/ml, the original cell seeding density to be consistent with the cell density obtained at time zero after performing a Hoechst nuclear stain and confocal microscopy on printed sheets (**Fig. S12**). No cell or biomaterials clumps or aggregates were observed immediately following printing, indicating that the delivered cells remain uniformly dispersed within the biomaterial.

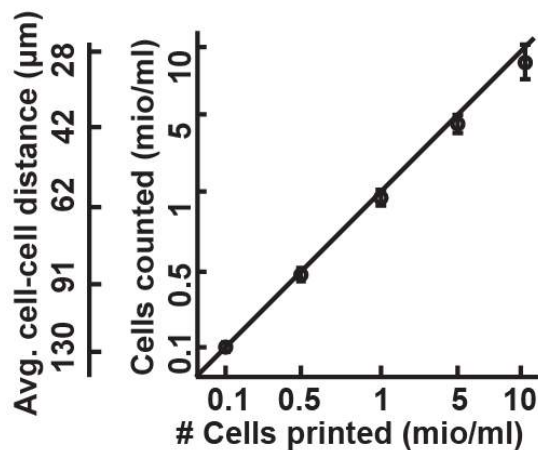


**Figure S12.** Various concentrations of cells were printed in bioink and quantified using Hoechst nuclear staining, demonstrating consistency and homogeneity in total cell number during deposition.

## S6. Porcine Wound Model Wound Area and Histological Analysis

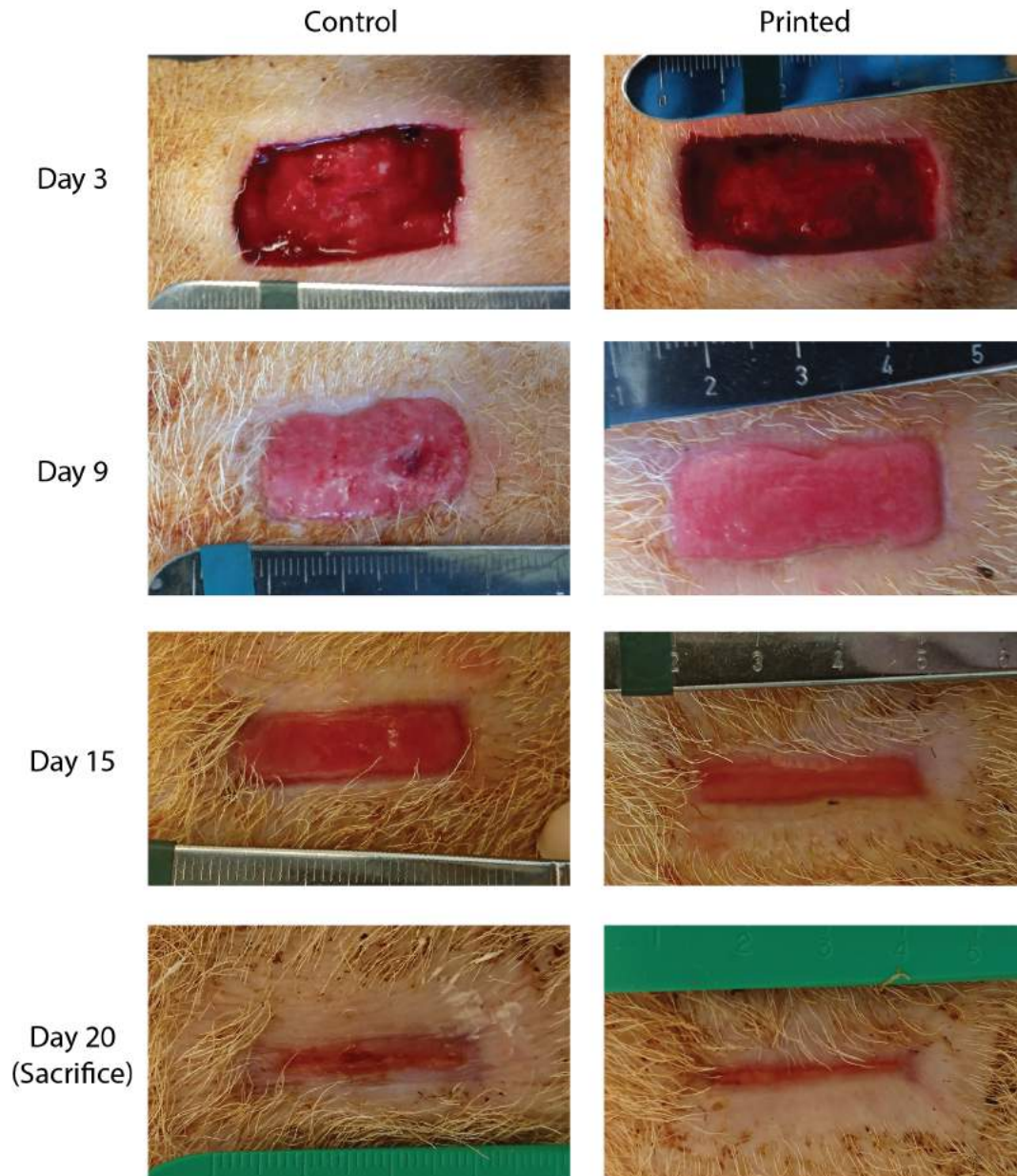


**Figure S13.** Representative bright field images of the wound area, comparing contralateral 4×2 cm<sup>2</sup> excisional wounds until the sacrifice day (Day 20). Only 1 of the 4 control wounds showed complete re-epithelialization while 3 out of 4 treated wounds exhibited complete re-epithelialization (non-significant parametric test).

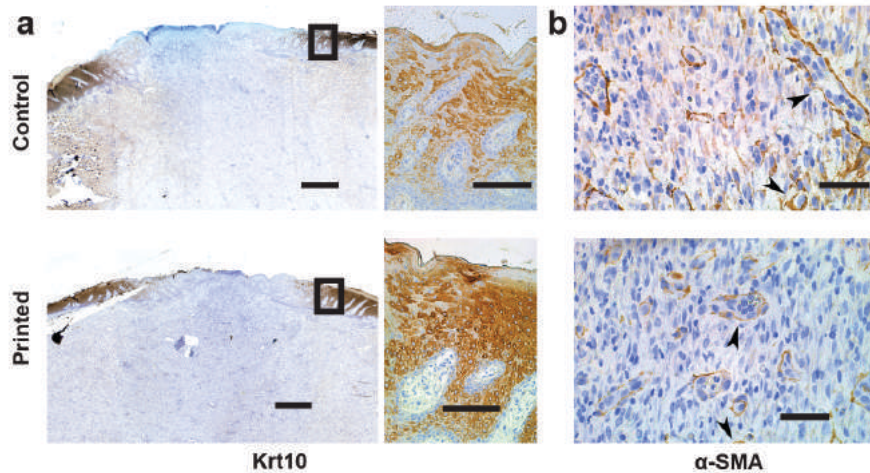


**Figure S14.** (a) Keratin 10 staining indicating comparable extent of differentiated keratinocytes. Increased number of keratin positive cells observed at wound edge. (b)  $\alpha$ -SMA staining reveals comparable number of positive cells in both printed and control wounds. Scale bars 1 mm (a, left), 100  $\mu$ m (a, right), and 50  $\mu$ m (b).

#### Supplementary References

1. D. Tremblay, C. M. Cuerrier, L. Andrzejewski, E. R. O'Brien and A. E. Pelling, *JoVE (Journal of Visualized Experiments)*, 2014, e51454-e51454.
2. M. N. Nicholas, M. G. Jeschke and S. Amini-Nik, *Tissue Eng Part A*, 2016, **22**, 754-764.
3. C. D. Murray, *Proc Natl Acad Sci U S A*, 1926, **12**, 207-214.
4. D. R. Emerson, K. Cieřlicki, X. Gu and R. W. Barber, *Lab on a Chip*, 2006, **6**, 447-454.
5. G. K. Batchelor, *An introduction to fluid mechanics*, Cambridge University Press, 1976.